Materials Advances

ROYAL SOCIETY OF CHEMISTRY

PAPER

View Article Online
View Journal | View Issue

Cite this: *Mater. Adv.*, 2021, **2**, 511

Investigating the formation of diverse ZnO nanostructures based on solvent, temperature, and pH as adjustable parameters†

Smriti Thakur and Sanjay K. Mandal *

Employing a coordination polymer, namely, $[Zn_2(bpma)_2(adc)_2]_n$, as a single-source precursor, the fabrication of diverse ZnO nanostructures with a variation in the morphologies and dimensionalities has been achieved through different processing parameters – solvent, pH and temperature. For example, 0D nanospheres and 1D nanorods have been obtained from the use of different solvents (methanol, ethanol, THF, toluene and hexane). Similarly, 3D nanoflowers composed of 1D nanorods with different aspect ratios have been obtained at two different temperatures (120 °C and 150 °C) as a result of their growth time. Furthermore, a systematic evolution of 3D nanoflowers assembled by nanosheets has been studied in different pH (9–12) conditions. The structural composition and surface morphology of the as-synthesized ZnO nanostructures was investigated by X-ray diffractometry (XRD), field emission spectroscopy (FESEM), transmission electron microscopy (TEM). The solid-state UV-vis diffuse reflectance spectra of the as-synthesized ZnO nanostructures showed absorption in the range of 363–383 nm with band gap values of 3.01–3.21 eV. Further, the photoluminescence spectra of the diverse ZnO nanostructures exhibited blue emission bands in the range of 410–460 nm, which originates from the intrinsic defect states of zinc interstitials, zinc vacancies and oxygen vacancies.

Received 9th October 2020,
Accepted 28th November 2020

DOI: 10.1039/d0ma00781a

rsc.li/materials-advances

Introduction

Nanostructured ZnO materials form an important class of semiconductor materials. ZnO is a well-known n-type semiconductor with a bandgap of 3.4 eV and a large free excitation binding energy (60 meV).[1,2] Furthermore, ZnO is relatively environment friendly because it is non-toxic and does not give out toxic products during the growth process.[3] It is also biocompatible.[4,5] Numerous strategies to control and monitor the size, dimensionality, and morphology of ZnO nanomaterials have been introduced due to their role in determining the magnetic, electrical, optical, and other properties.[6–11]

ZnO nanostructures having diverse morphologies have received enormous attention for their potential use in high performance devices.[12] There are numerous reports where ZnO has been produced with different morphologies by various synthetic methods: vapor–liquid–solid (VLS) processes, chemical vapor deposition (CVD), and thermal evaporation are three methods that have been used for fabricating one-dimensional ZnO nanowires or wire arrays onto different substrates. There are many other approaches that have been used to achieve other ZnO nanostructures, such as hydrothermal methods,[13] solvothermal methods,[14] sol–gel processes,[15] laser-induced decomposition,[16] ultrasonic irradiation methods,[17] microwave irradiation techniques[18] and vapor phase transport.[19] Among all these techniques, solution-based chemical routes, such as hydro-/solvothermal methods are the most prominent and effective processes. These provide an excellent control over stoichiometry, compositional modification, morphology, size and shape of nanostructures with inexpensive equipments – a key in this area. Therefore, a low-cost and simplified hydrothermal route has been adopted for the synthesis of ZnO nanostructures which offers several advantages in terms of operational simplicity, reliability, repeatability, low temperature, scalability, low cost, ease of composition control and complex procedures restrict further development in actual applications. Since hydrothermal synthesis is very much sensitive to the growth parameter variations,[20–24] the change and control of parameters – solvent, temperature and pH – can be successfully used for controlling the morphology of the nanostructures (Fig. 1). Other factors like growth process[25] and reactant concentration[26] also significantly control the morphology of the as-synthesized nanostructures. Thus, the synthesis of various morphologies of ZnO can be achieved by understanding the influence of each parameter

Department of Chemical Sciences, Indian Institute of Science Education and Research Mohali, Sector 81, Manauli PO, S.A.S. Nagar, Mohali, Punjab, 140306, India. E-mail: sanjaymandal@iisermohali.ac.in

† Electronic supplementary information (ESI) available: Lattice parameters, band gap values, SEM and TEM images. See DOI: 10.1039/d0ma00781a

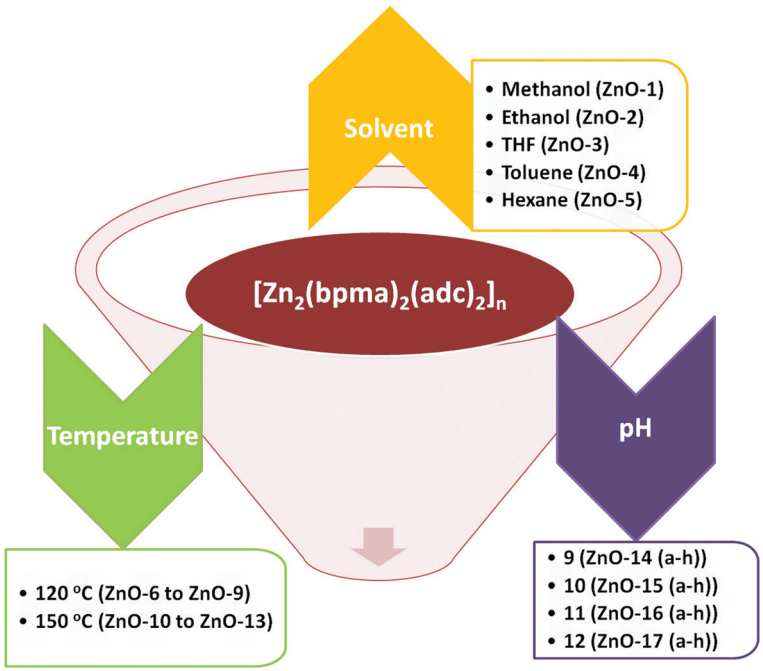

Fig. 1 Schematic representation of a systematic variation of solvent, temperature and pH for fabricating diverse ZnO nanostructures.

during the growth process. In this regard, the choice of a solvent can help in influencing the crystallization process as well as the shape (affecting the aspect ratio) of ZnO nanoparticles.[27] The surface morphology and porosity of ZnO nanostructures are important for the optoelectronic and electrical properties.[28–30]

In the present work, we report the synthesis of hierarchical ZnO nanostructures *via* the solvent, temperature and pH assisted hydrothermal method utilizing a water soluble coordination polymer (CP) $[Zn_2(bpma)_2(adc)_2]_n$ as the single-source precursor. A diversity in the daughter ZnO nanostructures has been obtained from the utilization of one parent CP. The novelty of this work is not only to achieve diverse ZnO nanostructures – 0D nanospheres, 1D nanorods, 2D nanosheets and 3D nanoflowers, from a solution-based hydrothermal method but also to investigate the effect of parameters – solvent, temperature and pH on their formation. These ZnO nanostructures can be utilized in optoelectronics and high performance devices. For example, ZnO nanoflowers with a star like structure composed of nanorods can be used in optoelectronic devices and solar cells,[31] and ZnO nanoparticles can be active materials for gas sensor applications.[32] Whereas, ZnO microflowers can act as a scattering layer for ZnO-based dye-sensitized solar cells with enhanced conversion efficiency,[33] and as antimicrobial agents against *Escherichia coli*.[34] Furthermore, the single-source precursor use in the formation of diverse nanostructures is rare and remarkable compared to the literature reports with modified procedures and precursors to achieve desired morphologies.

Experimental section

The analytical grade chemicals used in this work were obtained from commercial sources. These were used as received without further purification. $[Zn_2(bpma)_2(adc)_2]_n$ was prepared in gram quantities following the reported method.[35]

Synthesis of ZnO-1 to ZnO-5 in different solvents

For a general reaction, 0.05 mmol of $[Zn_2(bpma)_2(adc)_2]_n$ (39 mg) was added in five 3 mL Teflon reactors containing 2 mL of different solvents (methanol, ethanol, tetrahydrofuran (THF), toluene, hexane). The hydrothermal reactions were carried out at 180 °C for 24 hours. The reaction mixtures were centrifuged at 4000 rpm for 15–20 minutes for separating the solid followed by washing it several times with solvents employed for synthesis. The solids collected at the bottom of centrifuge tubes were dried at 60 °C for 6 hours to obtain the powdered ZnO particles of fine size.

Synthesis of ZnO-6 to ZnO-13 at different temperatures

Using 0.05 mmol (39 mg) of $[Zn_2(bpma)_2(adc)_2]_n$ and 3 mL of basic aqueous solution containing 120 mg (2.13 mmol) of KOH at a pH = 13 in 5 mL Teflon reactors, the hydrothermal reactions were carried out at two different temperatures (120 °C and 150 °C) for different time intervals (6, 12, 18 and 24 hours). The reaction mixtures were centrifuged at 4000 rpm for 15 minutes for separating the solid followed by washing it several times with ethanol. The solids collected were then dried at 60 °C for 8–10 hours to get the fine powdered ZnO particles.

Synthesis of ZnO-14 (a–h) to ZnO-17 (a–h) at different pH

Using 5 mL Teflon reactors, 0.05 mmol (39 mg) of $[Zn_2(bpma)_2(adc)_2]_n$ and 3 mL of water containing an appropriate amount of KOH were mixed to attain pH 9, 10, 11 or 12. The hydrothermal reactions were carried out at 180 °C for different time intervals (30 minutes to 12 hours). The

as-synthesized mixtures were then centrifuged at 4000 rpm for 15 minutes to separate the solids followed by washing them several times with ethanol. These solids, which were collected at the bottom of centrifuge tubes, were then dried at 60 °C for 6–8 hours to obtain the powdered ZnO particles.

Instrumentation

The morphology and chemical composition of the as-synthesized ZnO samples were examined using field-emission scanning electron microscopy (FE-SEM, JEOL, 15 kV). Powder X-ray diffraction (PXRD) patterns were recorded with a Rigaku Ultima IV diffractometer as described earlier.[36] The transmission electron microscopy (TEM) was performed on JEOL JEM F200 equipped with a field emission gun operate at 200 kV with 1 mg sample well dispersed in MeOH (10 mL) using a sonicator for 2 minutes and then put on the copper grid, which was allowed to dry using a lamp for 30 minutes. Solid state fluorescence spectra were obtained using a HORIBA Fluorolog 3 spectrofluorometer equipped with a Xenon lamp. Each data set was analyzed with FluorEssence™ software.

Results and discussion

Synthesis and structural characterization

Effect of solvent (ZnO-1 to ZnO-5). A solvent dependent study was carried out in different solvents (MeOH, EtOH, THF, toluene and hexane) at 180 °C for 24 hours using $[Zn_2(bpma)_2(adc)_2]_n$ to yield ZnO nanostructures (Scheme 1).

Different morphologies were obtained with the variation in the solvent based on the different polarity, saturated vapor pressure and boiling point of the solvents.[37] The ZnO nanostructures obtained with the variation in the solvents were characterized by powder diffraction technique. All the samples exhibited hexagonal wurtzite phase of ZnO (JCPDS 06-2151). The sharpness of the intense peaks obtained confirms the purity of the structures (Fig. 2). The as-obtained ZnO nanostructures exhibited high crystallinity and purity. Using eqn (1), the calculated lattice parameters are given in Table S1 (ESI†).[38]

$$\frac{1}{d^2} = \frac{4}{3}\left(\frac{h^2 + hk + k^2}{a^2}\right) + \frac{l^2}{c^2} \quad (1)$$

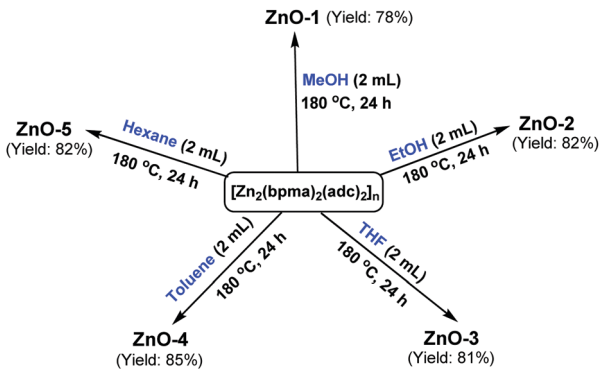

Scheme 1 Synthesis of **ZnO-1** to **ZnO-5** in different solvents.

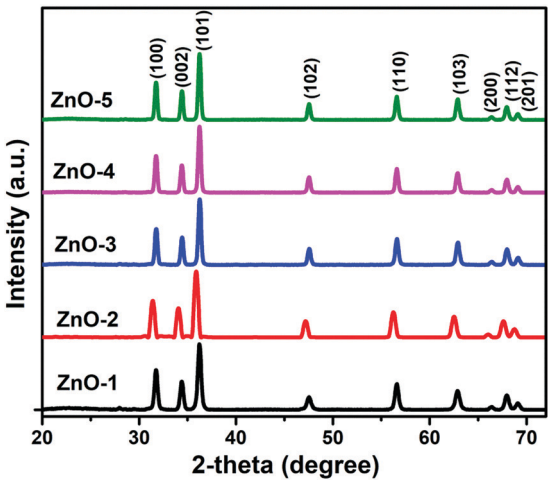

Fig. 2 PXRD patterns of **ZnO-1** to **ZnO-5**.

where h, k, and l are the Miller indices, d is the interplanar spacing, and a and c represent the lattice parameters. The interplanar spacing for the plane (h k l) can be calculated from Bragg's law: $2d \sin\theta = n\lambda$. Based on $V = 0.866a^2c$, the volume of the hexagonal unit cell was determined while the atomic packing fraction of the nanostructures was calculated using eqn (2). These values are also listed in Table S1 (ESI†).

$$\text{Atomic packing fraction (A.P.F.)} = \frac{2\pi a}{3\sqrt{3}c} \quad (2)$$

Effect of temperature (ZnO-6 to ZnO-13). ZnO nanostructures were synthesized at different temperatures (120 and 150 °C) using $[Zn_2(bpma)_2(adc)_2]_n$ and KOH. The synthesis was carried out hydrothermally for different times (6 hours, 12 hours, 18 hours and 24 hours) in basic conditions at pH > 13 (Scheme 2). The star shaped ZnO nanostructures made of nanorods were obtained. The time dependent study at two different temperatures resulted in variation of the aspect ratio of nanorods of these nanostructures.

The diffraction patterns of ZnO nanorods grown with different aging times (6 h, 12 h, 18 h and 24 h) at different temperatures 120 °C and 150 °C (**ZnO-6** to **ZnO-13**) were obtained (Fig. 3) to determine the crystalline phase of the nanorods. The 2θ values of diffraction peaks obtained are in good agreement with the standard JCPDS data for ZnO (JCPDS 06-2151).

The ZnO nanorods contain only hexagonal wurtzite structure as the crystalline phase. The formation of nanorods with wurtzite structure could be attributed to the anisotropic growth along (001) plane owing to a faster growth velocity in this direction under hydrothermal conditions. The higher intensity of the (101) diffraction peak in all the patterns further provides the evidence of the preferential growth direction along the c-axis.[13] No other traces of impurity were observed in the reflection peaks indicating high purity of the obtained nanorods. The strong and narrow peaks further revealed good crystallinity of the rods. For this set of ZnO nanostructures,

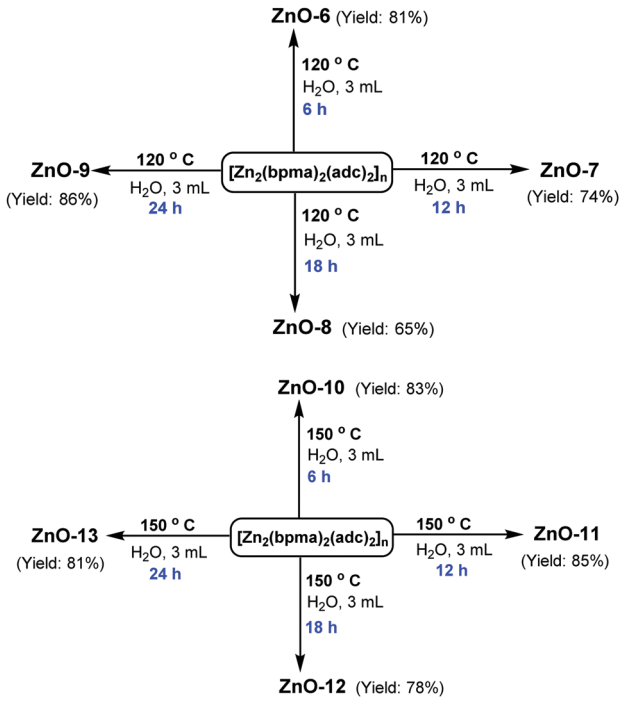

Scheme 2 Synthesis of **ZnO-6** to **ZnO-13** with a variation in time and temperature.

the lattice parameters, volume and atomic packing fractions are listed in Table S2 (ESI†).

Effect of pH (ZnO-14 (a–h) to ZnO-17 (a–h)). ZnO nanostructures have also been synthesized at different pH varying from 9 to 12 employing Zn(II) coordination polymer $[Zn_2(bpma)(adc)_2]_n$. The hydrothermal reaction was carried out at 180 °C in 3 mL of water containing KOH at pH ranging from 9 to 12 (Scheme 3). The reaction was carried out for different aging times from 30 minutes to 12 hours with a gap of 60 minutes to monitor the growth of ZnO micro flowers. The as-obtained ZnO micro flowers obtained after 12 hours of aging time were characterized by PXRD technique. The peaks obtained in the spectra could be clearly indexed to hexagonal wurtzite structure of ZnO (JCPDS 06-2151). The sharp and intense peaks confirm the purity of the obtained samples (Fig. 4). No other impurity peak has been obtained which further confirms the purity of the ZnO nanostructures. For this set of ZnO nanostructures, the lattice parameters, volume and atomic packing fractions are provided in Table S3 (ESI†).

Microscopic analysis and mechanism of formation

ZnO-1 to ZnO-5 nanostructures. The surface morphology of the ZnO nanostructures obtained in different solvents was studied by FESEM (Fig. 5). ZnO nanoparticles of size 7–10 nm were obtained in case where methanol has been used as the solvent. Whereas, nanoparticles of size 15–25 nm were observed in ethanol. However, tetrahydrofuran (THF) with high boiling point yielded nanoflowers composed of nanorods with aspect ratio 4.72. In case of toluene also, the bullet-like nanorods with sharp tips at the end were obtained with aspect ratio of

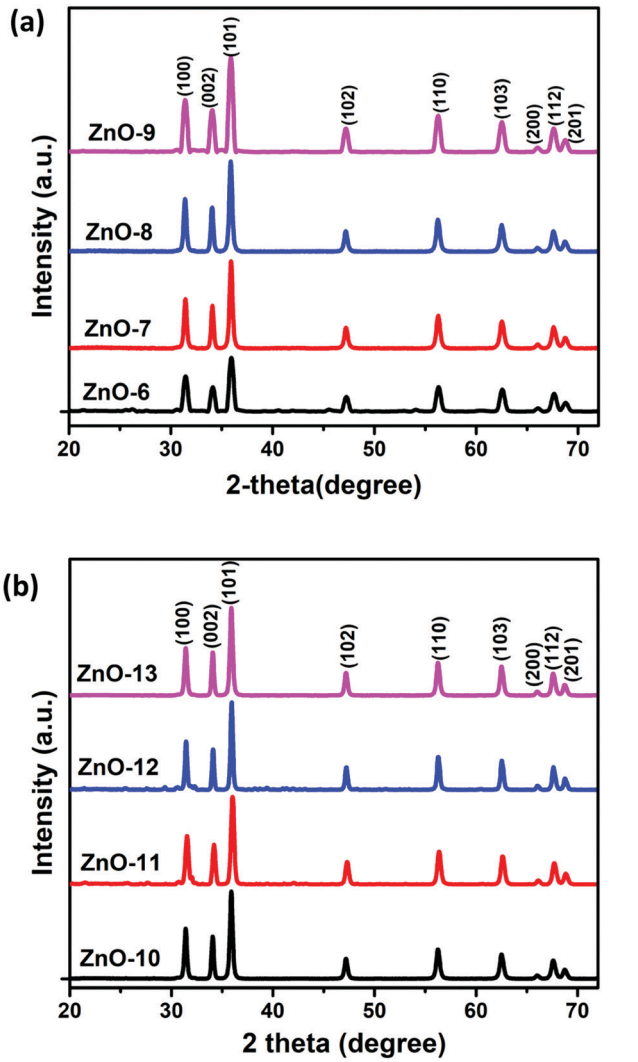

Fig. 3 PXRD patterns of (a) **ZnO-6** to **ZnO-9** and (b) **ZnO-10** to **ZnO-13**.

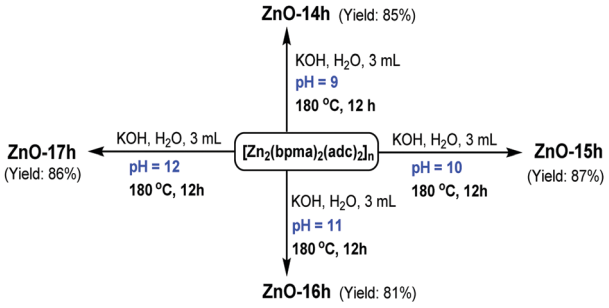

Scheme 3 Synthesis of **ZnO-14h** to **ZnO-17h** with a variation in pH.

5. On the other hand, hexane yielded nanoparticles of size 30–40 nm as shown in Scheme 4. Thus, it has been observed that low boiling point solvents (ethanol, methanol and hexane) resulted in producing the spherical structures and high boiling point solvents resulted in giving 1D nanorods.[39,40] In general, the initial nucleation of the crystals and the solubility of the

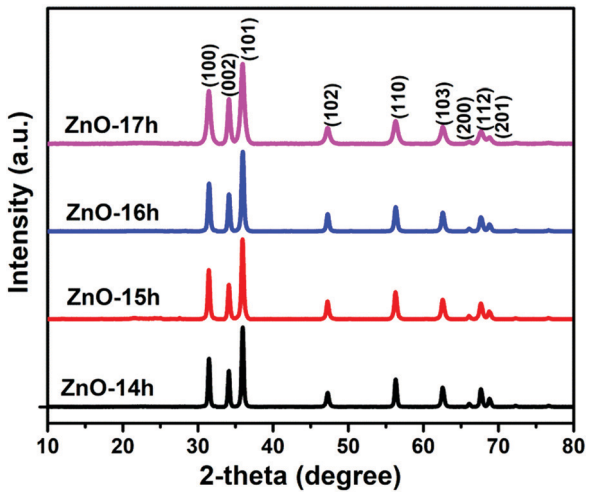

Fig. 4 PXRD patterns of **ZnO-14h** to **ZnO-17h**.

precursor in the solvents play a crucial role in contributing to the overall morphology of the products. Under the hydrothermal conditions, the saturated vapor pressure and boiling points of the solvents are inversely related to each other.[41]

The boiling points of toluene, THF, ethanol, hexane and methanol are 111, 66, 78, 68, and 65, respectively. Thus, the saturated vapor pressures of these solvents follow the reverse order. A high saturated vapor pressure of the solvents like methanol, ethanol and hexane resulted in a limited growth of ZnO nuclei which gives rise to substantial nucleation of particles. The nanoparticles aggregated by clustering together to reduce the overall surface energy. On the other hand, when the solvents such as toluene and THF were used, which have relatively low saturated vapor pressures, anisotropic growth was favored to yield ZnO nanorods. The nanoparticles aggregated by clustering together to reduce the overall surface energy. On the other hand, when the solvents such as toluene and THF were used, which have relatively low saturated vapor pressures, anisotropic growth was favored to yield ZnO nanorods. A similar study where water was used as the solvent gave varied ZnO nanostructures on changing the amount of water, particularly 3D microflowers in 2 mL water.[36] Therefore, the above results clearly indicated the role of saturated vapor pressure of the solvent in producing the ZnO nanostructures with different morphologies as shown in Table 1.

The structural features of ZnO nanostructures were further investigated by TEM measurements for **ZnO-2** (Fig. 6) and **ZnO-4** (Fig. 7). The nanoparticles of size in the range 15–25 nm are clearly visible in **ZnO-2**. Whereas, in case of **ZnO-4**, the nanorods were formed. The lattice spacing in nanospheres (**ZnO-2**) was found to be 0.258 nm while that in nanorods (**ZnO-4**) was found to be 0.269 nm. The selected area electron diffraction patterns confirm the presence of diffraction planes obtained from their XRD patterns (Fig. 6c and 7c).

ZnO-6 to ZnO-13 nanostructures. A series of experiments were carried out at 120 °C and 150 °C for different duration from 6 hours to 24 hours to synthesize the star like ZnO nanostructures composed of nanorods with different aspect ratios. Fig. 8 and 9 show the typical FESEM images of the as-grown ZnO nanorods at 120 °C and 150 °C. The structures composed of more than 10 nanorods were observed at all the temperatures. The nanorods in **ZnO-6** obtained at 120 °C have a typical length of 1.04 μm and diameter of 300 nm (Fig. 9). As the hydrothermal time was increased to 12 hours, the rods get broader and longer (A.R. ∼ 3.53). The lengthening of the rods continued for 18 hours as shown in Table 2. However, at the end of 24 hours a decrease in length as well as diameter was observed which might be due to dissolution of Zn^{2+} ions in the system from the ends.

At 150 °C, a high aspect ratio of the nanorods has been achieved. The solubility of the crystallites increased as the temperature increased leading to a higher growth rate at 150 °C compared to 120 °C. Furthermore, the length and the diameter of the rods increased on extending the growth time

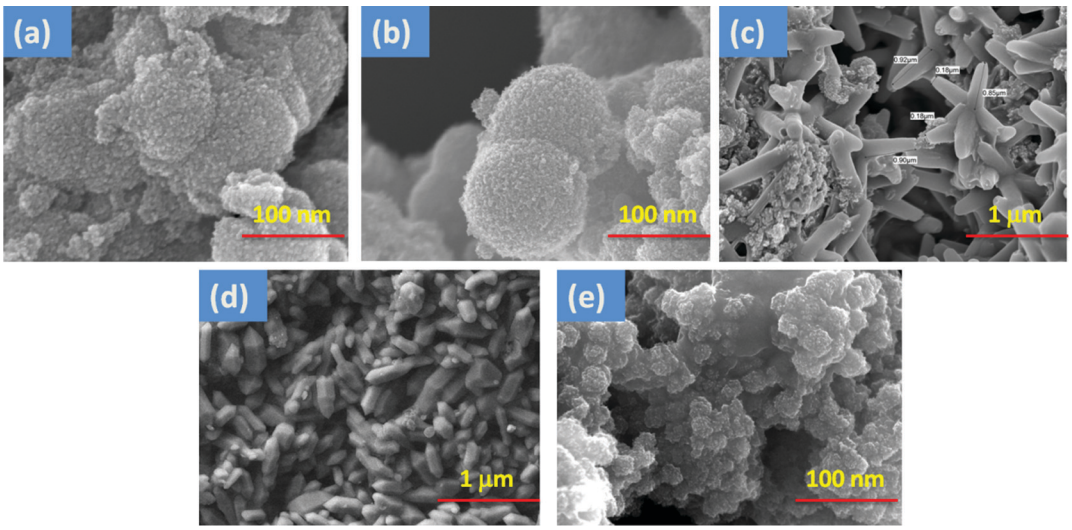

Fig. 5 ZnO nanostructures (**ZnO-1** to **ZnO-5**) obtained in different solvents: (a) methanol, (b) ethanol, (c) THF, (d) toluene and (e) hexane.

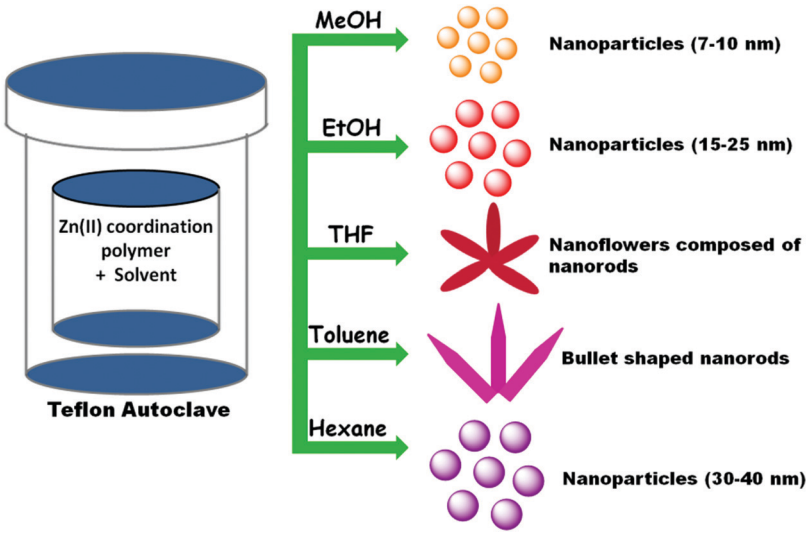

Scheme 4 Growth mechanism of ZnO nanostructures in different solvents.

Table 1 Morphologies of ZnO nanostructures obtained in different solvents

Sample	Solvent	Boiling point	Morphology
ZnO-1	Methanol	65	Nanoparticles (7–10 nm)
ZnO-2	Ethanol	78	Nanoparticles (15–25 nm)
ZnO-3	THF	66	Nanorods
ZnO-4	Toluene	111	Nanorods
ZnO-5	Hexane	68	Nanoparticles (30–40 nm)

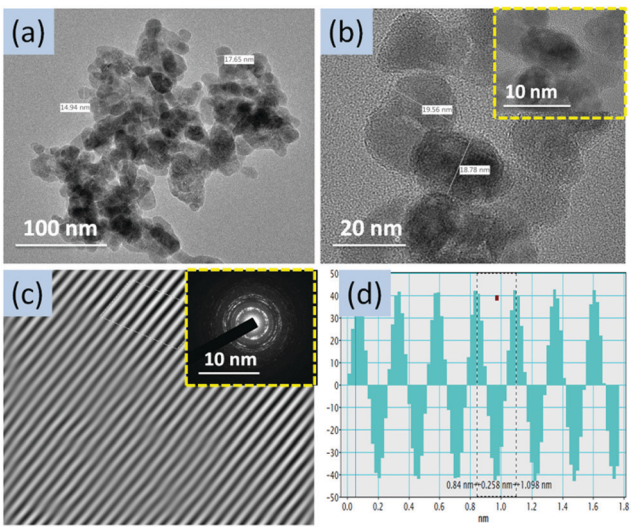

Fig. 6 (a) TEM image at 100 nm, (b) TEM image at 20 nm (inset: HRTEM image at 10 nm), (c) lattice fringe (inset: SAED pattern) and (d) *d*-spacing average of **ZnO-2**.

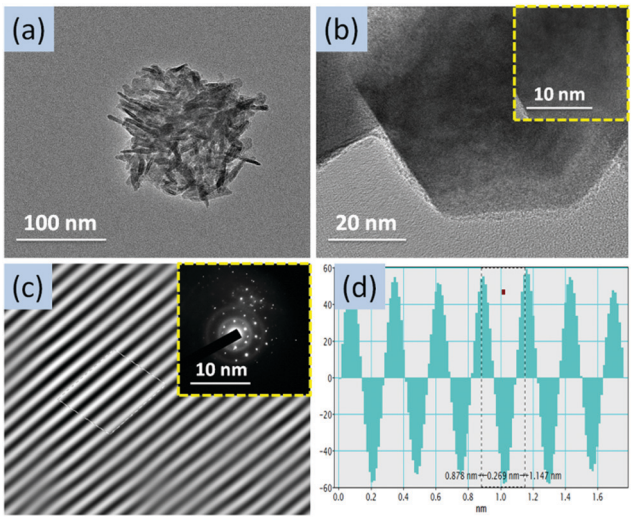

Fig. 7 (a) TEM image at 100 nm, (b) TEM image at 20 nm (inset: HRTEM image at 10 nm), (c) lattice fringe (inset: SAED pattern) and (d) *d*-spacing average of **ZnO-4**.

from 6 hours to 12 hours (Fig. 8). The length and diameter of the rods continued to increase up to 18 hours (Table 2).

Fig. 10 shows the TEM images of **ZnO-8** at the end of 18 hours where nanorods are clearly visible in Fig. 10a and b. The SAED pattern in Fig. 10c confirms the presence of diffraction planes obtained from XRD pattern. The lattice spacing was found to be 0.267 nm as shown in Fig. 10d. The nanorods with less aspect ratio in **ZnO-9** were also observed in TEM results (Fig. S1, ESI†) which clearly proves the results obtained in SEM.

The average length and diameter of the rods produced at 150 °C is more than that at 120 °C (Fig. 9). The self-assembly of the nanorods arrays produced get self-assembled by interweaving of the rods to produce 3D nanoflowers thus reducing the overall surface energy to achieve thermodynamic stability.[42]

The trend for the increase in the aspect ratios with the extension of growth time is also similar in this case. The growth time controls the length of the nanorods.[43] A longer rod is produced with longer growth duration up to a certain time.

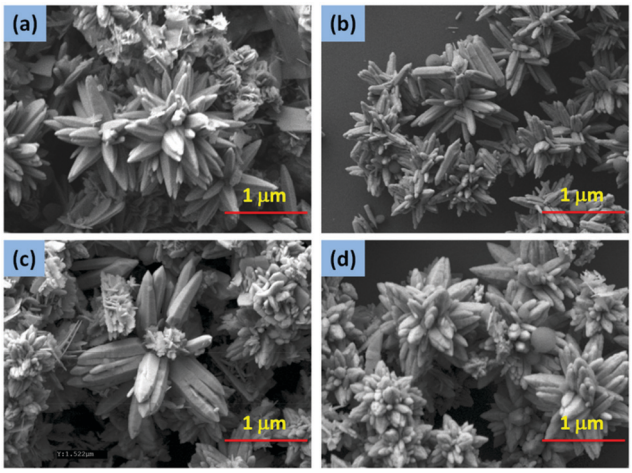

Fig. 8 Star-like ZnO nanostructures composed of nanorods with different aspect ratios (a) **ZnO-6**, (b) **ZnO-7**, (c) **ZnO-8** and (d) **ZnO-9**.

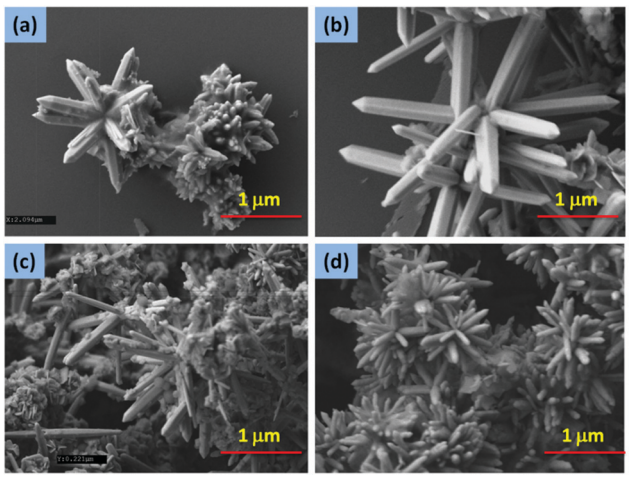

Fig. 9 Star-like ZnO nanostructures composed of nanorods with different aspect ratios (a) **ZnO-10**, (b) **ZnO-11**, (c) **ZnO-12** and (d) **ZnO-13**.

Table 2 Aspect ratios of ZnO nanorods (**ZnO-6** to **ZnO-13**)

Sample	Length (μm)	Diameter (μm)	Aspect ratio
ZnO-6	1.04	0.30	3.46
ZnO-7	1.38	0.39	3.53
ZnO-8	1.81	0.44	4.11
ZnO-9	1.03	0.41	2.56
ZnO-10	2.18	0.45	4.84
ZnO-11	2.41	0.49	4.91
ZnO-12	3.19	0.55	5.80
ZnO-13	1.02	0.22	4.63

On further increase of growth time, a decrease in the aspect ratio of the rods due to dissolution of the tips of the rods at the ends can be observed. The experimental results suggest that temperature and growth time control the aspect ratio of nanorods. In this work, the effect of temperature (with different growth times) on the aspect ratio of the nanorods has been

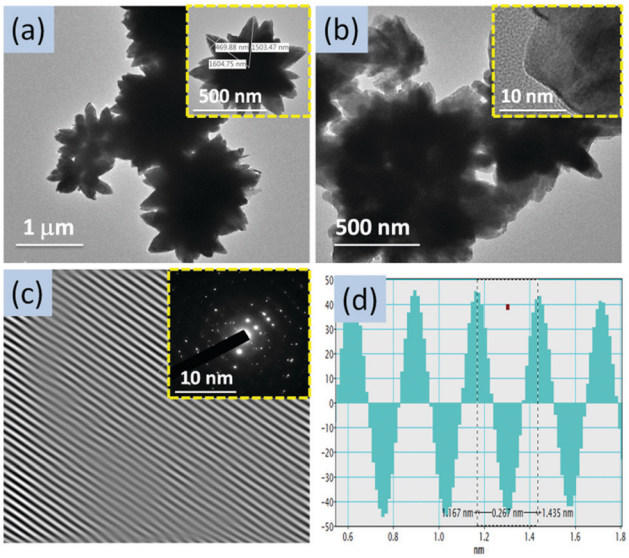

Fig. 10 (a) TEM image at 1 μm (inset: TEM image at 500 nm), (b) TEM image at 500 nm (inset: HRTEM image at 10 nm), (c) lattice fringe (inset: SAED pattern) and (d) *d*-spacing average of **ZnO-8**.

investigated in detail. In order to control and design the rods with tailored aspect ratios it is imperative to understand the growth mechanism of these rods. The internal structure as well as the external conditions such as temperature, growth time, *etc.* are the important parameters in influencing the growth of a crystal.

The chemical reactions involved in the hydrothermal conditions are shown in eqn (3)–(5):

$$Zn^{2+} + 2OH^- \rightarrow Zn(OH)_2 \quad (3)$$

$$Zn(OH)_2 + 2OH^- \rightarrow [Zn(OH)_4]^{2-} \quad (4)$$

$$[Zn(OH)_4]^{2-} \rightarrow ZnO + H_2O + 2OH^- \quad (5)$$

$[Zn(OH)_4]^{2-}$ acts as the growth unit for the formation of ZnO nanorods where a number of dissolution–nucleation cycles evolves the nanorods.[44–46] The different growth rate of planes are: $V_{0001} > V_{\bar{1}0Mx\bar{0}31;Mx\bar{0}031;} > V_{\bar{1}010} > V_{\bar{1}011} > V_{000\bar{1}}$. The higher growth rate along (0001) direction results in rapid disappearance of this plane leading to a pointed shape at the end of the *c*-axis, which explains the formation of rods with pointed tips at the ends giving star like ZnO nanostructures. After a certain time, these rods unite with other neighboring rods to evolve into flower-like structures by reducing their surface energy. It has been observed that temperature plays a significant role in tuning the dimensions and aspect ratios of these rods. A higher temperature (150 °C) and an optimized growth time of 18 hours resulted in giving the rods with high aspect ratios, whereas a comparatively less aspect ratios of rods was observed at lower temperature of 120 °C (Scheme 5). Also, a lowering of aspect ratios after 18 hours was observed in both the cases. Thus, the temperature as well as the growth time helped in manipulating and tailoring the length and diameter of these rods.

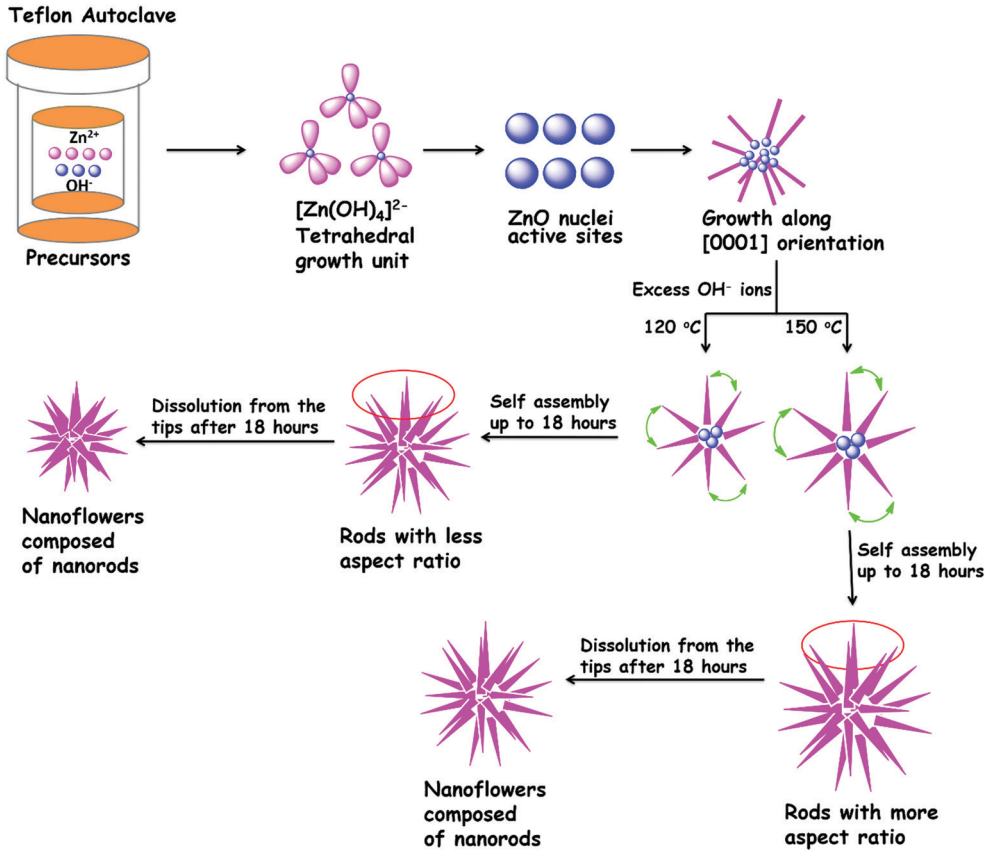

Scheme 5 Growth mechanism of nanoflowers composed of nanorods at different temperatures.

The TEM images (Fig. 11) of **ZnO-12** clearly shows the nanorods with more aspect ratio compared to **ZnO-9** nanorods. The SAED pattern in Fig. 11c also confirms the presence of diffraction planes obtained from XRD pattern. The lattice spacing was found to be 0.283 nm as shown in Fig. 13d. The similar results were obtained for **ZnO-13** with low aspect ratio as compared to **ZnO-12** (Fig. S2, ESI†). The above result for **ZnO-6** to **ZnO-13** adds additional data points to those observed at 180 °C.[34]

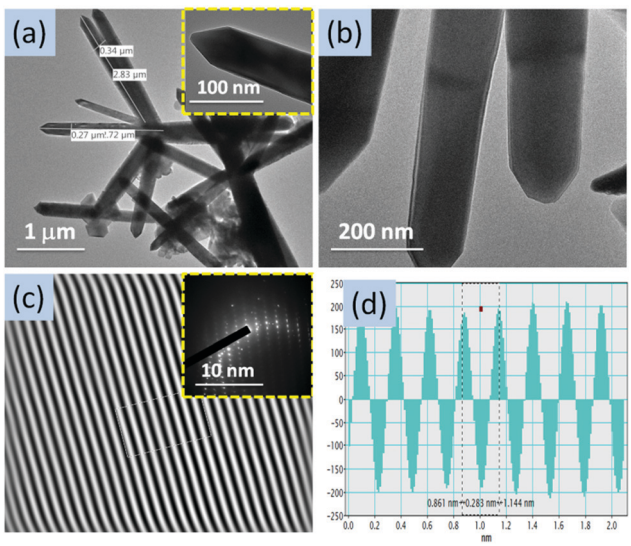

Fig. 11 (a) TEM image at 1 μm (inset: TEM image at 100 nm), (b) TEM image at 200 nm, (c) lattice fringe (inset: SAED pattern) and (d) *d*-spacing average of **ZnO-12**.

ZnO-14 (a–h) to ZnO-17 (a–h) nanostructures. The surface analysis of the ZnO nanostructures obtained at different pH conditions was analyzed by FESEM. The nanostructures were synthesized for different aging times to observe the overall evolution of microflowers (Fig. 12). Initially, the two-dimensional growth in the reaction mixture was observed for the first 2 hours with the formation of nanosheets. These nanosheets started getting assembled with the neighboring nanosheets to form 3D flowers to lower their surface energy (Scheme 6). At the end of 4 hours, the formation of flowers could be clearly observed except in the case of pH = 11 and pH = 12 where 1D rods were also obtained along with 2D sheets due to the presence of a greater number of OH^- ions compared to the previous two cases. The sheets unite together with neighboring sheets to form 3D flowers by decreasing the overall surface energy. The optimized time for the evolution of full bloom flowers were observed to be 12 hours in each case shown in Fig. S3–S5 (ESI†). After extending the synthesis time, not much change has been observed in the overall morphology of the ZnO microflowers. These results at different pH are summarized in Table 3.

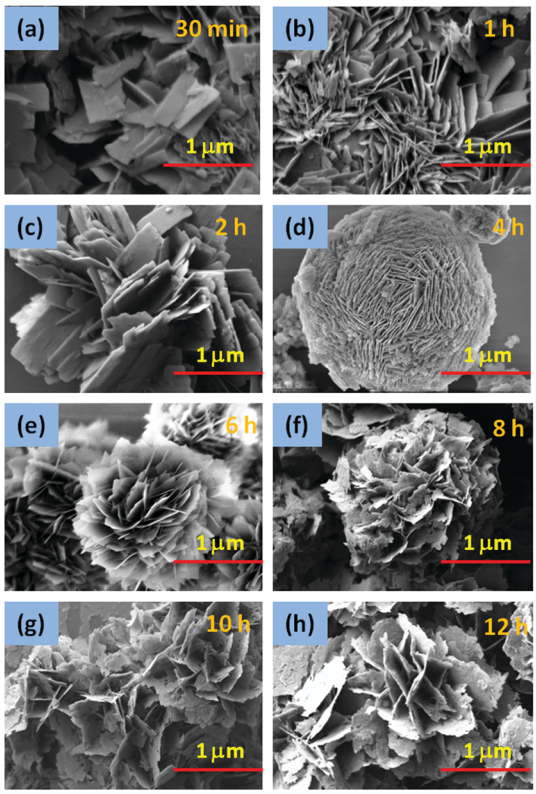

Fig. 12 (a–h) Formation of 3D ZnO nanoflowers (at pH = 9) assembled by nanosheets as a result of growth time from 30 minutes to 12 hours.

The structural features of ZnO nanostructures obtained at different pH conditions were further confirmed by TEM measurements. Fig. 13, 14 and 16 show the flower-like ZnO nanostructures obtained at the end of 12 hours at pH = 9, 10 and 12, whereas ZnO nanorods (Fig. 15) have been shown which were obtained at the end of 4 hours at pH = 11. The SAED patterns in the TEM images (Fig. 13–16) confirm the results obtained from the XRD patterns. The lattice spacing were found to be 0.28 nm, 0.323 nm, 0.179 nm and 0.278 nm in **ZnO-14h**, **ZnO-15h**, **ZnO-16d** and **ZnO-17h**, respectively.

Optical properties

ZnO-1 to ZnO-5 nanostructures. UV-vis diffuse reflectance spectra of the as-synthesized ZnO nanostructures were recorded in order to investigate their optical properties. The spectra of these nanostructures showed the maximum absorption in the UV region[47,48] 365–370 nm followed by a sharp decrease (Fig. 17). This blue shift in the absorption spectra of these nanostructures compared to that of bulk ZnO[49,50] (378 nm) is due to their respective sizes obtained in the nanorange. The bandgap energies of these nanostructures were obtained using the following equation:

$$\alpha(h\nu)^{1/n} = B(h\nu - E_{gap}) \quad (6)$$

where α is the absorption coefficient, $h\nu$ is the photon energy, B is the band form parameter, E_{gap} is the optical band gap of the nanoparticles and n is an index whose value depends on the type of transition in the process of absorption. The graph between $(\alpha h\nu)^2$ *vs.* $h\nu$ gives the energy band gap values when the linear portions of the spectra were extrapolated to x-axis. The band gap values for **ZnO-1** to **ZnO-5** are listed in Table S4 (ESI†).

ZnO-6 to ZnO-13 nanostructures. UV-vis diffuse reflectance spectra of the as-synthesized ZnO nanorods at different temperatures in the wavelength range of 300–600 nm are shown in

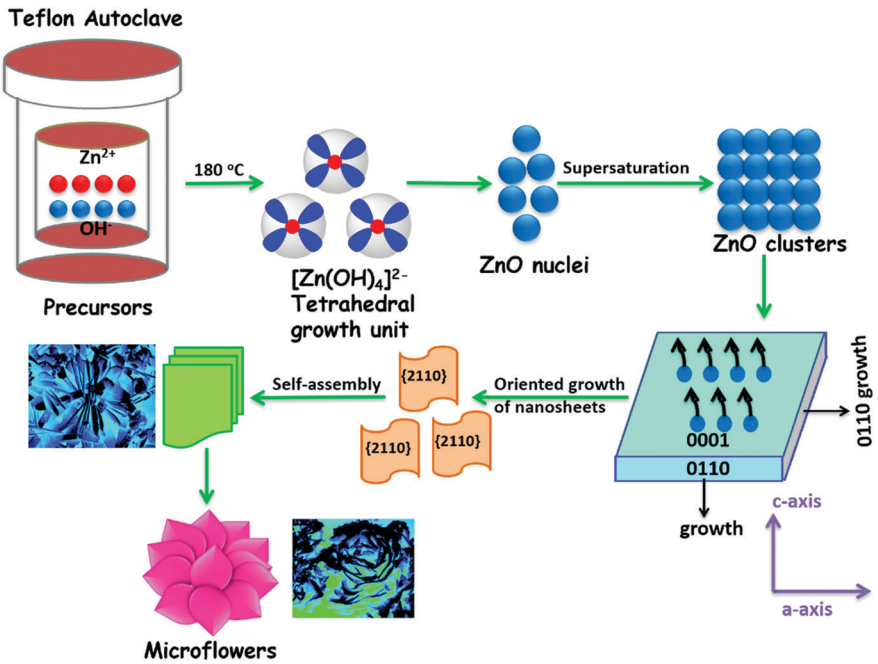

Scheme 6 Mechanism of transformation of nanosheets to microflowers.

Table 3 Morphologies of ZnO nanostructures obtained at different pH

Sample	pH	Time	Morphology
ZnO-14 (a–h)	9	30 minutes to 12 hours	Nanosheets to microflowers
ZnO-15 (a–h)	10	30 minutes to 12 hours	Nanosheets to microflowers
ZnO-16 (a–h)	11	30 minutes to 12 hours	Nanosheets to nanorods to microflowers
ZnO-17 (a–h)	12	30 minutes to 12 hours	Nanosheets to nanorods to microflowers

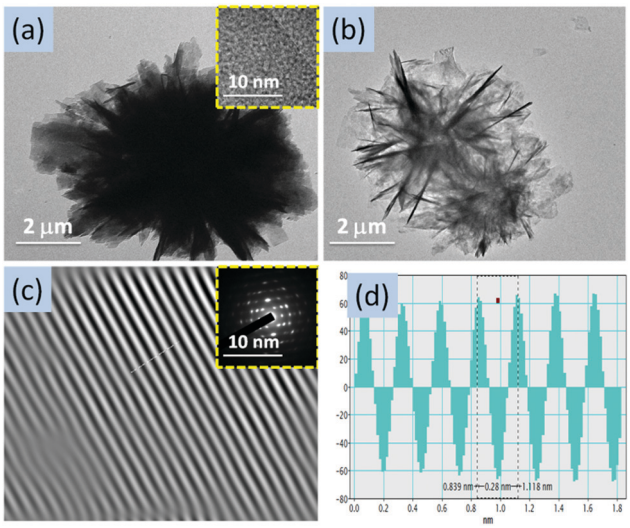

Fig. 13 (a) TEM image at 2 μm (inset: HRTEM image at 10 nm), (b) TEM image at 2 μm, (c) lattice fringe (inset: SAED pattern) and (d) *d*-spacing average of **ZnO-14h** obtained at pH = 9 at the end of 12 hours.

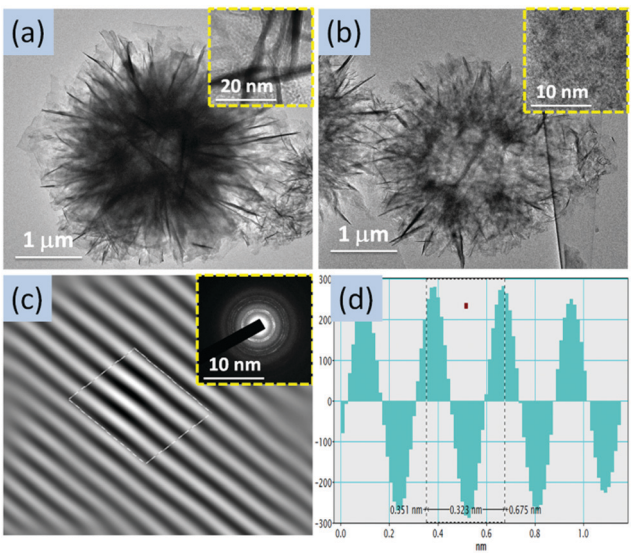

Fig. 14 (a) TEM image at 1 μm (inset: HRTEM image at 20 nm), (b) TEM image at 1 μm (inset: HRTEM image at 10 nm), (c) lattice fringe (inset: SAED pattern) and (d) *d*-spacing average of **ZnO-15h** obtained at pH = 10 at the end of 12 hours.

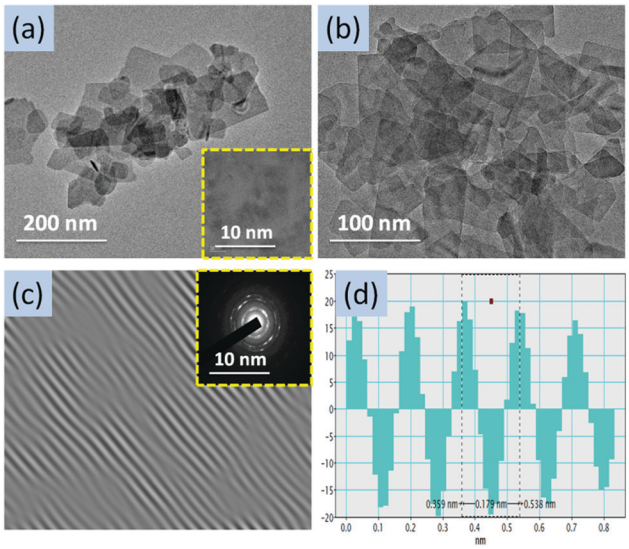

Fig. 15 (a) TEM image at 200 nm (inset: HRTEM image at 10 nm), (b) TEM image at 100 nm, (c) lattice fringe (inset: SAED pattern) and (d) *d*-spacing average of **ZnO-16d** obtained at pH = 11 at the end of 4 hours.

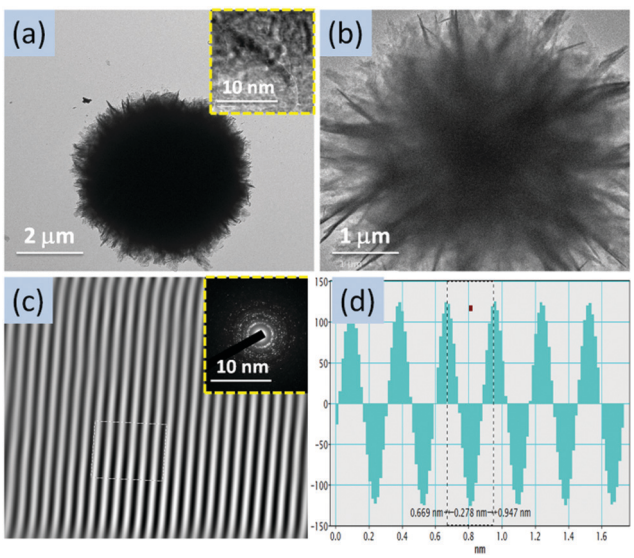

Fig. 16 (a) TEM image at 2 μm (inset: HRTEM image at 10 nm), (b) TEM image at 1 μm, (c) lattice fringe (inset: SAED pattern) and (d) *d*-spacing average of **ZnO-14h** obtained at pH = 12 at the end of 12 hours.

Fig. 18. The spectra at different temperatures observed for different growth duration showed the absorption edge between 363–368 nm followed by a sharp decrease. The blue shift in the absorption spectra with respect to the bulk absorption edge at

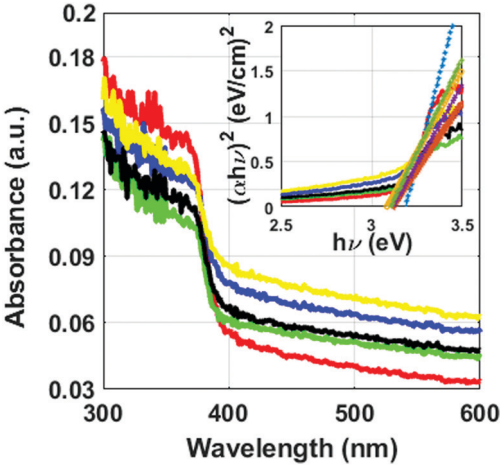

Fig. 17 Solid state diffuse reflectance spectra of **ZnO-1** to **ZnO-5** (color code: red, **ZnO-1**; green, **ZnO-2**; blue, **ZnO-3**; black, **ZnO-4** and magenta, **ZnO-5**); (inset) a plot of $(\alpha h\nu)^2$ *versus* $(h\nu)$.

378 nm is attributed to the effect of nanocrystalline size of the synthesized nanorods. A slight shift in the absorption edges has been observed for ZnO nanorods with different growth duration. There is a blue shift in the absorption spectra for the nanorods with lower diameters. Since rods with lower diameters were observed with longer growth time. Thus, the blue shift in the absorption edge increases slightly with increasing growth time. Furthermore, the rods with increasing growth time from 6 hours to 18 hours also showed an increase in the intensities of their absorption except the case of rods obtained with 24 hours.

Since the rods with minimum aspect ratios has been obtained at the end of 24 hours; a minimum intensity has been observed in this case and the highest peak of excitonic absorption were observed for the nanorods with a growth time of 18 hours. The higher defect density of the nanorods on their surfaces resulted in different binding energies which explain the reason of the spectral shift in the nanorods. The band gap energies of the ZnO nanorods was calculated using Tauc relation (eqn (6)). The band gap values for **ZnO-6** to **ZnO-13** are listed in Table S5 (ESI†).

ZnO-14 (a–h) to ZnO-17 (a–h) nanostructures. UV-vis diffuse reflectance of the as-synthesized ZnO nanostructures was recorded in the wavelength range of 200–800 nm to study the absorption properties of the structures and also to obtain the band gap values. In the spectra, ZnO nanostructures (**ZnO-14h** to **ZnO-17h**) exhibited highest absorption band around 368 nm, which confirms a strong binding in the obtained nanostructures (Fig. 19).

The characterization of the energy band gap (E_g) values for the **ZnO-14h** to **ZnO-17h** was done using Tauc relation (eqn (6)). Though the energy band gap values were found to be very close to each other but an increasing trend in the values has been observed with the increase of pH values. The values were found to be 3.13 eV for **ZnO-14h**, 3.14 eV for **ZnO-15h**, 3.17 eV for **ZnO-16h** and 3.21 eV for **ZnO-17h**.

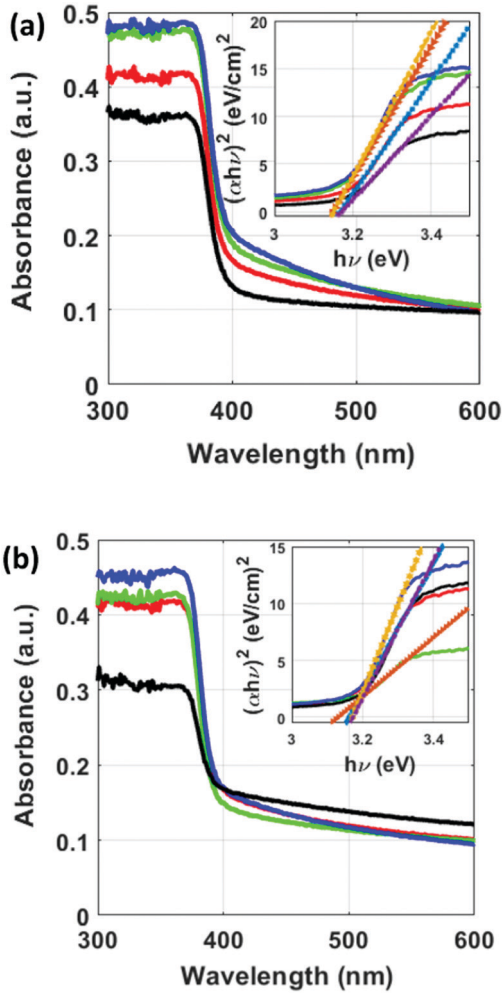

Fig. 18 Solid state diffuse reflectance spectra of (a) **ZnO-6** to **ZnO-9** (color code: red, **ZnO-6**; green, **ZnO-7**; blue, **ZnO-8** and black, **ZnO-9**), (b) **ZnO-10** to **ZnO-13** (color code: red, **ZnO-10**; green, **ZnO-11**; blue, **ZnO-12** and black, **ZnO-13**); (inset) a plot of $(\alpha h\nu)^2$ *versus* $(h\nu)$.

Photoluminescence properties

ZnO-1 to ZnO-5 nanostructures. In order to understand the luminescent properties of the ZnO nanostructures obtained in different solvents, the experiments were carried out at an excitation wavelength of 350 nm. **ZnO-1** showed three emission bands in the blue region of the visible spectrum whereas in case of **ZnO-2** and **ZnO-3**, a broad blue emission band in the range of 410–460 nm has been obtained (Fig. 20). Furthermore, similar results have been obtained for **ZnO-4** except that the blue region of the spectrum is a bit wider. On the other hand, **ZnO-5** showed a similar result to **ZnO-2** and **ZnO-3**. The intrinsic defects present in ZnO in the form vacancies of zinc and oxygen[51–53] show blue emission as a result of recombination of charge carriers.

ZnO-6 to ZnO-13 nanostructures. The room temperature photoluminescence of the as-grown ZnO nanorods at different temperatures (120 °C and 150 °C) were carried out using xenon lamp as the source at an excitation wavelength of 350 nm. The spectra were recorded in the wavelength range of 380 to

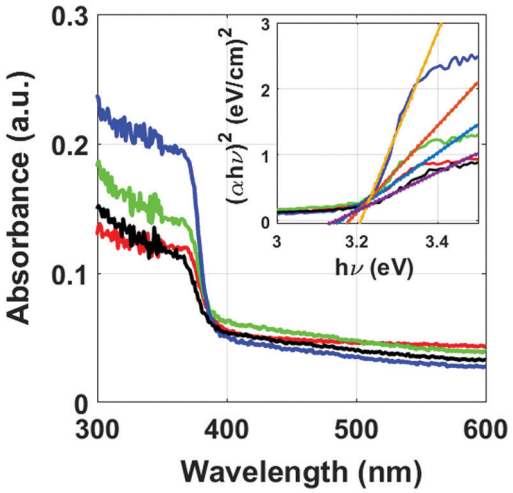

Fig. 19 Solid state diffuse reflectance spectra of **ZnO-14h** to **ZnO-17h** (color code: red, **ZnO-14h**; green, **ZnO-15h**; blue, **ZnO-16h** and black, **ZnO-17h**); (inset) a plot of $(\alpha h\nu)^2$ *versus* $(h\nu)$.

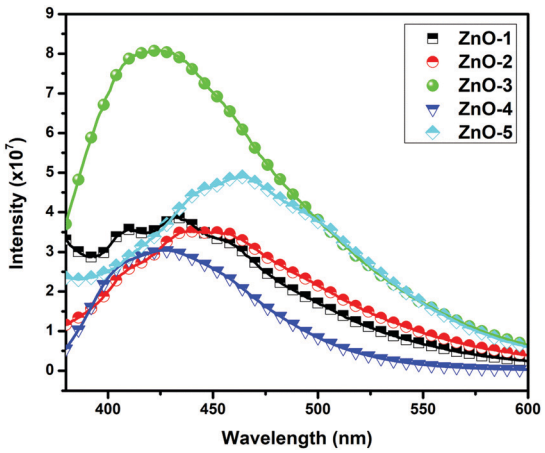

Fig. 20 Photoluminescence spectra of **ZnO-1** to **ZnO-5**.

600 nm. A broad emission band in the visible range of the spectra could be clearly observed for the as grown ZnO nanorods (Fig. 21a). The strong blue emission band within a range of 410–430 nm for the ZnO nanorods is mainly caused due to the defects resulted from the zinc interstitials, zinc vacancies and oxygen vacancies.[51–54]

The electronic transition from either the Zn_i to valence band or from the bottom of conduction band to O_i level resulted in blue emission of these nanorods. With the increase of aspect ratios from 6 hours to 18 hours, a significant increase in the intensity of emission has also been observed in all the cases (**ZnO-6** to **ZnO-8**) at 120 °C. However, a decrease in the emission intensity has been observed for **ZnO-9** obtained with a growth time of 24 hours. A similar trend has been observed at 150 °C for different growth times (**ZnO-9** to **ZnO-13**) as shown in Fig. 21b. Thus, the nanorods with higher aspect ratios can show intense emission in the visible range ensuring the exploitation of these rods in the light emitting devices.[55]

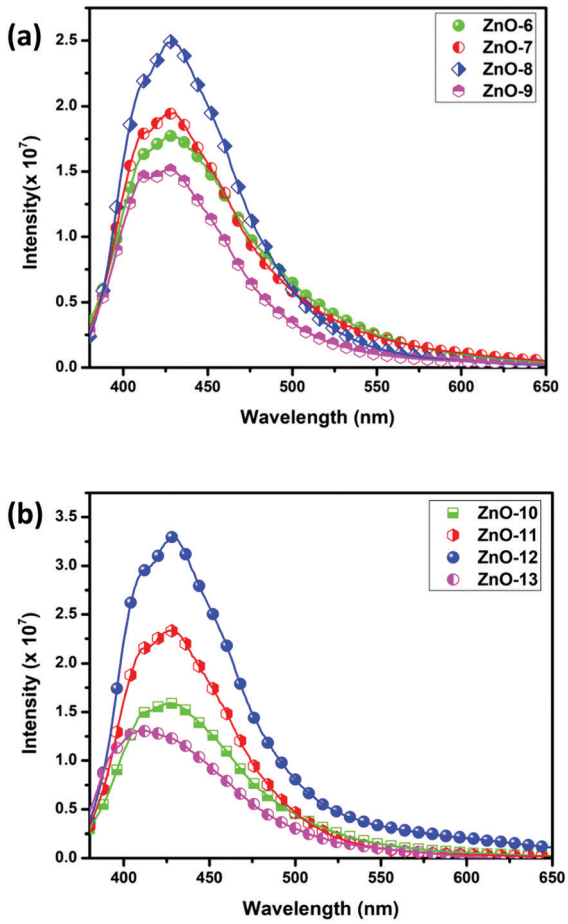

Fig. 21 Photoluminescence spectra of (a) **ZnO-6** to **ZnO-9** and (b) **ZnO-10** to **ZnO-13**.

ZnO-14 (a–h) to ZnO-17 (a–h) nanostructures. The photoluminescence measurements were carried out on the as-obtained ZnO nanostructures (**ZnO-14h** to **ZnO-17h**) at an excitation wavelength of 350 nm. A broad blue emission band in the range of 400–430 nm could be clearly observed in all the nanostructures.

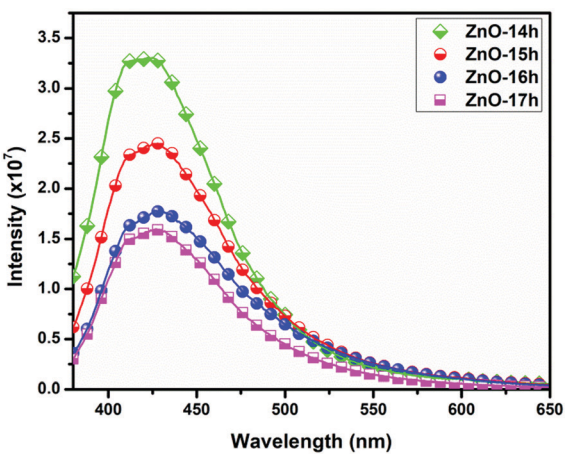

Fig. 22 Photoluminescence spectra of **ZnO-14h** to **ZnO-17h**.

This blue emission is attributed to the intrinsic defects present in ZnO (zinc vacancies and oxygen vacancies) nanostructures.[50–52] A decrease in the intensities has been observed for the structures synthesized in more basic conditions with a greater value of pH as illustrated in Fig. 22. The ZnO nanostructures obtained at pH = 9 showed the maximum intensity of absorption whereas a decreasing trend has been observed with increase in pH conditions from 10 to 12.

Conclusions

In summary, this work presented the formation of ZnO nanostructures using a single source precursor in different solvent (methanol, ethanol, THF, toluene and hexane), temperature (120 °C and 150 °C) and pH conditions (9–12). Different morphologies and dimensionalities of ZnO nanostructures have been obtained. For example, 0D nanospheres and 1D nanorods have been obtained with the variation in the solvents based on their boiling points. Whereas, 3D nanoflowers composed of 1D nanorods have been obtained based on the variation in their hydrothermal temperatures. A difference in the aspect ratios of these nanorods was observed as a result of their growth time at two different temperatures. Further, 3D nanoflowers assembled by 2D nanosheets have been obtained in different pH conditions (9–12). A systematic growth of the formation of these flowers up to 12 hours has been demonstrated. UV-vis spectra of these ZnO nanostructures showed an absorption in the range of 360–370 nm. Furthermore, broad blue emission bands in the range of 410–460 nm have been obtained for the ZnO nanostructures as a result of recombination of charge carriers originating from the zinc vacancies and oxygen vacancies.

Conflicts of interest

There are no conflicts to declare.

Acknowledgements

Funding for this work was provided by IISER, Mohali. S. T. is grateful to MHRD of India for a research fellowship. The X-ray, FESEM, HRTEM and other departmental facilities at IISER Mohali, are gratefully acknowledged.

Notes and references

1 W. Il Park, G. C. Yi, M. Kim and S. J. Pennycook, *Adv. Mater.*, 2003, **15**, 526–529.
2 J.-K. Song, M.-B. Zheng, Z.-J. Yang, H.-Q. Chen, H. Y. Wang, J. S. Liu, G. B. Ji, H.-Q. Zhang and J.-M. Cao, *Nanoscale Res. Lett.*, 2009, **4**, 1512–1516.
3 S. Singh, K. C. Barick and D. Bahadur, *Nanomater. Nanotechnol.*, 2013, **3**, 57237.
4 J. W. Rasmussen, E. Martinez, P. Louka and D. G. Wingett, *Expert Opin. Drug Delivery*, 2010, **7**, 1063–1077.
5 Y. Zhang, T. Nayak, H. Hong and W. Cai, *Curr. Mol. Med.*, 2013, **13**, 1633–1645.
6 M. A. Garcia, J. M. Merino, E. F. Pinel, A. Quesada, J. De La Venta, M. L. R. González, G. R. Castro, P. Crespo, J. Llopis, J. M. González-Calbet and A. Hernando, *Nano Lett.*, 2007, **7**, 1489–1494.
7 J. H. Lee, K. H. Ko and B. O. Park, *J. Cryst. Growth*, 2003, **247**, 119–125.
8 A. B. Djurišić, A. M. C. Ng and X. Y. Chen, *Prog. Quantum Electron.*, 2010, **34**, 191–259.
9 P. Nuengmatcha, S. Chanthai, R. Mahachai and W. C. Oh, *J. Environ. Chem. Eng.*, 2016, **4**, 2170–2177.
10 S. J. Jeong, H. S. Moon, J. Shin, B. H. Kim, D. O. Shin, J. Y. Kim, Y. H. Lee, J. U. Kim and S. O. Kim, *Nano Lett.*, 2010, **10**, 3500–3505.
11 G. D. Yuan, W. J. Zhang, J. S. Jie, X. Fan, J. X. Tang, I. Shafiq, Z. Z. Ye, C. S. Lee and S. T. Lee, *Adv. Mater.*, 2008, **20**, 168–173.
12 L. M. Al-Harbi, E. H. El-Mossalamy, H. M. Arafa, A. Al-Owais and M. A. Shah, *Mod. Appl. Sci.*, 2011, **5**, 87–91.
13 S. Xu, Y. Wei, M. Kirkham, J. Liu, W. Mai, D. Davidovic, R. L. Snyder and L. W. Zhong, *J. Am. Chem. Soc.*, 2008, **130**, 14958–14959.
14 R. Razali, A. K. Zak, W. H. A. Majid and M. Darroudi, *Ceram. Int.*, 2011, **37**, 3657–3663.
15 S. A. Kamaruddin, K. Y. Chan, H. K. Yow, M. Zainizan Sahdan, H. Saim and D. Knipp, *Appl. Phys. A: Mater. Sci. Process.*, 2011, **104**, 263–268.
16 C. Fauteux, R. Longtin, J. Pegna and D. Therriault, *Inorg. Chem.*, 2007, **46**, 11036–11047.
17 A. Hajnorouzi, R. Afzalzadeh and F. Ghanati, *Ultrason. Sonochem.*, 2014, **21**, 1435–1440.
18 S. Cho, S. H. Jung and K. H. Lee, *J. Phys. Chem. C*, 2008, **112**, 12769–12776.
19 A. Bakin, A. Che Mofor, A. El-Shaer and A. Waag, *Superlattices Microstruct.*, 2007, **42**, 33–39.
20 G. Amin, M. H. Asif, A. Zainelabdin, S. Zaman, O. Nur and M. Willander, *J. Nanomater.*, 2011, **2011**, 1–9.
21 R. Wahab, S. G. Ansari, Y. S. Kim, M. Song and H. S. Shin, *Appl. Surf. Sci.*, 2009, **255**, 4891–4896.
22 S. Xu, C. Lao, B. Weintraub and Z. L. Wang, *J. Mater. Res.*, 2008, **23**, 2072–2077.
23 S. Das, K. Dutta and A. Pramanik, *CrystEngComm*, 2013, **15**, 6349–6358.
24 S. Zhu, X. Chen, F. Zuo, M. Jiang, Z. Zhou and D. Hui, *J. Solid State Chem.*, 2013, **197**, 69–74.
25 Y. Wang, T. Jiang, D. Meng, J. Yang, Y. Li, Q. Ma and J. Han, *Appl. Surf. Sci.*, 2014, **317**, 414–421.
26 T. Jiang, Y. Wang, D. Meng, X. Wu, J. Wang and J. Chen, *Appl. Surf. Sci.*, 2014, **311**, 602–608.
27 P. Tonto, O. Mekasuwandumrong, S. Phatanasri, V. Pavarajarn and P. Praserthdam, *Ceram. Int.*, 2008, **34**, 57–62.
28 J. Zhang, L. Sun, J. Yin, H. Su, C. Liao and C. Yan, *Chem. Mater.*, 2002, **14**, 4172–4177.
29 Y. J. Kwon, K. H. Kim, C. S. Lim and K. B. Shim, *J. Ceram. Process. Res.*, 2002, **3**, 146–149.

30 D. Chandra, S. Mridha, D. Basak and A. Bhaumik, *Chem. Commun.*, 2009, 2384–2386.
31 B. Kharisov, *Recent Pat. Nanotechnol.*, 2008, **2**, 190–200.
32 U. Manzoor, F. Tuz Zahra, S. Rafique, M. T. Moin and M. Mujahid, *J. Nanomater.*, 2015, 189058.
33 J. Xu, K. Fan, W. Shi, K. Li and T. Peng, *Sol. Energy*, 2014, **101**, 150–159.
34 S. Thakur and S. K. Mandal, *New J. Chem.*, 2020, **44**, 11796–11807.
35 S. Khullar and S. K. Mandal, *RSC Adv.*, 2014, **4**, 39204–39213.
36 S. Thakur and S. K. Mandal, *CrystEngComm*, 2020, **22**, 3059–3069.
37 B. Sikora, K. Fronc, I. Kaminska, A. Baranowska-Korczyc, K. Sobczak, P. Dłuzewski and D. Elbaum, *J. Sol-Gel Sci. Technol.*, 2012, **61**, 197–205.
38 T. Prakash, G. Neri, A. Bonavita, E. Ranjith Kumar and K. Gnanamoorthi, *J. Mater. Sci.: Mater. Electron.*, 2015, **26**, 4913–4921.
39 J. Xie, P. Li, Y. Li, Y. Wang and Y. Wei, *Mater. Lett.*, 2008, **62**, 2814–2816.
40 S. Kuriakose, B. Satpati and S. Mohapatra, *Adv. Mater. Lett.*, 2015, **6**, 1104–1110.
41 P. B. Khoza, M. J. Moloto and L. M. Sikhwivhilu, *J. Nanotechnol.*, 2012, **2012**, 1–6.
42 R. Shabannia, *Prog. Nat. Sci.: Mater. Int.*, 2015, **25**, 95–100.
43 A. Leelavathi, G. Madras and N. Ravishankar, *Phys. Chem. Chem. Phys.*, 2013, **15**, 10795–10802.
44 S. Xu and Z. L. Wang, *Nano Res.*, 2011, **4**, 1013–1098.
45 C. Wang, Y. Gao, L. Wang and P. Li, *Phys. Status Solidi A*, 2017, **214**, 201600876.
46 Y. Aditya Sumanth, R. Annie Sujatha, S. Mahalakshmi, P. C. Karthika, S. Nithiyanantham, S. Saravanan and M. Azagiri, *J. Mater. Sci.: Mater. Electron.*, 2016, **27**, 1616–1621.
47 Z. Wang, X. Qian, J. Yin and Z. Zhu, *Langmuir*, 2007, **20**, 3441–3448.
48 A. N. Redkin, L. Chow, I. M. Tiginyanu, G. Chai, V. V. Ursaki, G. A. Emelchenko, O. Lupan and A. N. Gruzintsev, *Sens. Actuators, B*, 2009, **144**, 56–66.
49 Y.-H. Hwang, B. Weng, C. Chang, H.-K. Kim, J. Qiu, Z. Shi, X. Li and L. Zhao, *J. Nanomater.*, 2014, **2014**, 1–11.
50 D. Segets, J. Gradl, R. K. Taylor, V. Vassilev and W. Peukert, *ACS Nano*, 2009, **3**, 1703–1710.
51 J. B. Xia and K. Cheah, *Phys. Rev. B: Condens. Matter Mater. Phys.*, 1997, **55**, 15688–15693.
52 A. Janotti and C. G. Van De Walle, *Phys. Rev. B: Condens. Matter Mater. Phys.*, 2007, **76**, 165202.
53 P. Erhart and K. Albe, *Appl. Phys. Lett.*, 2006, **88**, 201918.
54 C. Deng, N. Ma, M. Aravind, G. Wang, P. Yu, C. To, N. Hung and D. H. Ng, *Mater. Lett.*, 2004, **58**, 2195–2198.
55 D. K. Kwon, Y. Porte and J. M. Myoung, *J. Phys. Chem. C*, 2018, **122**, 11993–12001.